CHAPTER 5

Ni-Al Substituted $SrFe_{12-x-y}Ni_xAl_yO_{19}$ Series

5.1 Introduction

In the previous chapters, the M_s value of strontium hexaferrite was effectively improved, while the improvement in H_c is not very significant compared to the NdFeB. Al^{3+} ion is reported as the best non-rare-earth substitution that may reduce the gap of hard magnetism between strontium hexaferrite and NdFeB magnet. As shown in Fig 5.1, the substitution of four Al^{3+} ions is found to be very effective in enhancing the H_c of SrM. The highest H_c of 18.85 kOe is reported for $SrFe_8Al_4O_{19}$ with the sol-gel auto-combustion synthesis process (Shekhawat & Roy, 2019). It results in the H_c value of the SrM magnet being even higher than the NdFeB (Wang et al., 2012). However, there is a major drawback of Al substitution, which cause a sharp and drastic decline in M_s (HE et al., 2011; Luo et al., 2012; Sleptsova et al., 2021; Torkian et al., 2016; Trusov et al., 2018; Wang et al., 2012, 2017), which is not desirable for the objective of high $(BH)_{max}$. In addition to the Al^{3+} ion, substituting elements that can result in a high M_s value of SrM could be considered to compensate for this M_s drop. A few elements like Co (Roohani et al., 2017), Ni (Mousavi Ghahfarokhi et al., 2015), Zn (Abdellahi et al., 2018), Ti (Liu et al., 2019b) are found to result in high M_s in SrM magnet. Ni^{2+} ion is an economical (approximately $1/6^{th}$ of cobalt price) and low melting element than the Co^{3+} ion. It may also be effective in improving the magnetic properties of the Al-substituted SrM magnet with a low-cost choice and without adversely affecting the H_c of materials.

In this chapter, a composition of $SrFe_{12-x-y}Ni_xAl_yO_{19}$ [(x,y) = (0.005,1); (0.01,2); (0.015,3); (0.02,4); (0,1); (0.01,0)] is studied. The substitutional amount of Ni^{2+} ion is kept

very small up to 0.02 so that it only helps in M_s improvement without deteriorating the H_c of the material based on the reported behavior of Ni ion (Mousavi Ghahfarokhi et al., 2015). It will be favorable in improving the magnetism of strontium hexaferrite for the permanent magnet, especially for motor applications, because the featured rare-earth magnet application is moving towards switch reluctance or ferrite magnetic systems with the development of electric vehicles. In this chapter, the feasibility of enhancing magnetic properties in strontium hexaferrite has been further studied.

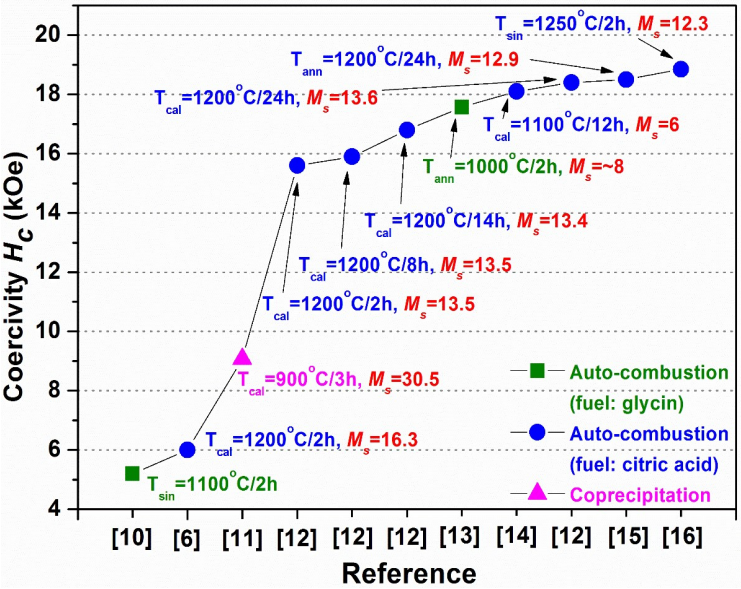

Figure 5.1 *Progress in coercivity (H_c, kOe) & saturation magnetization (M_s, emu/g) of $SrFe_8Al_4O_{19}$ hexaferrite with different synthesis parameters like T_{ann}, T_{cal}, and T_{sin}.*

5.2 Results and Discussion

5.2.1 Structural Properties

Fig. 5.2 shows the x-ray diffraction (XRD) patterns of auto-combustion synthesized $SrFe_{12-x-y}Ni_xAl_yO_{19}$ ($0.005 \leq x \leq 0.02$; $1 \leq y \leq 4$) calcined powder. All the resilient XRD peaks matched with the strontium hexaferrite peaks of ICDD card 79-1411 and indexed accordingly. The absence of any additional phase in the measuring range confirms the

formation of pure and well-crystallized hexagonal phases with a space group of $P6_3/mmc$. The values of structural parameters are listed in Table 5.1.

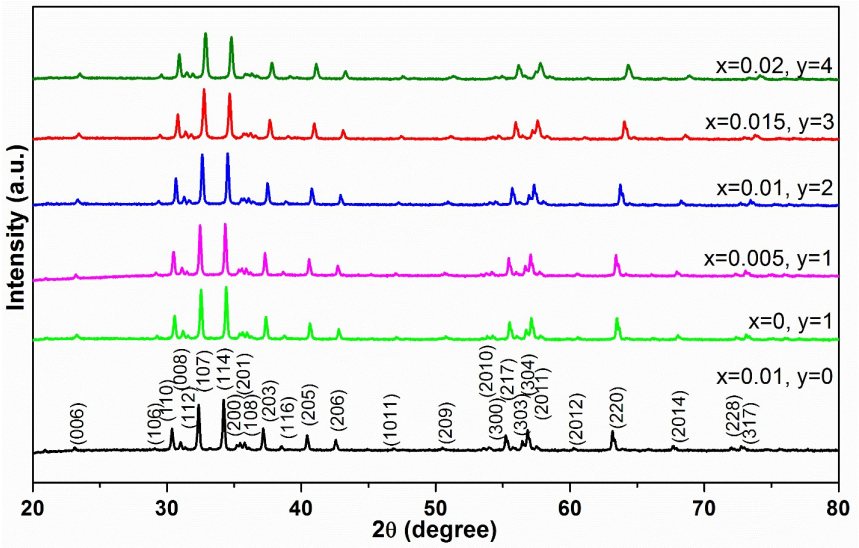

Figure 5.2 *XRD patterns of $SrFe_{12-x-y}Ni_xAl_yO_{19}$ ($0.005 \leq x \leq 0.02$; $1 \leq y \leq 4$) hexaferrites.*

Table 5.1 *Structural parameters of $SrFe_{12-x-y}Ni_xAl_yO_{19}$ ($0.005 \leq x \leq 0.02$; $1 \leq y \leq 4$) hexaferrites.*

Composition	Lattice Parameter		*c/a*	*V*	*D*	*Є*	*χD*
	a, b (Å)	*c* (Å)		(Å^3)	(nm)	(10^{-3})	(g/cm^3)
x=0.01, y=0	5.88	23.05	3.92	690.03	77.45	1.606	5.11
x=0, y=1	5.85	22.92	3.92	678.86	70.51	1.754	5.05
x=0.005, y=1	5.86	22.97	3.92	682.98	70.54	1.757	5.02
x=0.01, y=2	5.82	22.86	3.93	671.49	64.23	1.921	4.97
x=0.015, y=3	5.80	22.77	3.93	664.11	60.38	2.034	4.88
x=0.02, y=4	5.78	22.71	3.93	658.18	52.63	2.328	4.78

With the increase in Al^{3+} substitution content, a steady shift of XRD peaks towards the higher diffraction angle is observed in the material. It has resulted in the variation of lattice parameters, i.e., a decrease in *a* & *c* with the Al^{3+} ion content. Substitution of Al ion in the strontium hexaferrite structure decreases its interplanar spacing (d_{hkl}) (Torkian et al., 2016). According to Bragg's law ($\lambda = 2d \sin\theta$), any reduction in *d* would eventually lead

to the shift of θ values towards a higher angle. It is caused due to the large difference between ionic radii of Al^{3+} (0.51Å) and Fe^{3+} (0.64Å) ions (Wang et al., 2017). Replacement of Fe ion with smaller Al ion leads to a contraction in the unit cell and hence a reduction in unit cell volume. However, the small substitution of Ni ion does not show an evident effect in structural parameters as its ionic radius is 0.69Å (Roohani et al., 2018) which gives a small resultant change in ionic radii compared to Al ion. For the insight of structural quantification *c/a* ratio is calculated. The value of the *c/a* ratio is less than 3.98, which confirms a stable magnetoplumbite hexagonal structure of samples (Chen et al., 2008). The crystallite size of all the compositions is in the range of 52-78 nm. It is lesser to a huge extent than the critical single domain size of ~500 nm for pure strontium hexaferrite driven by Kittle's theory of single domain creation (Luo et al., 2012). The crystallite size of compositions decreases with the increase in Al ion content. Al ions substitution causes a reduction in unit cell volume, which decreases the mass transportation within the neighboring constituent part during crystal growth, resulting in smaller crystallite size. It can also be depicted by the broadening of reflection peaks, resulting in the reduction of crystallite size as reflected in XRD data (Liu et al., 2011). The crystallite size range endorses the formation of a single domain structure and narrow distribution of particles.

5.2.2 Spectroscopic Properties

FT-IR spectroscopy of desiccated calcined powder of $SrFe_{12-x-y}Ni_xAl_yO_{19}$ ($0.005 \leq x \leq 0.02$; $1 \leq y \leq 4$) in the range of 4000-400 cm^{-1} is shown in Fig. 5.3 for the insight of intermolecular chemical bond structure. There are three characteristic peaks in the FTIR spectrum of all the compositions. In M-type hexaferrite, the octahedral site attributes a 400-500 cm^{-1} band, while the tetrahedral site attributes a 500-700 cm^{-1} band due to Fe^{3+}-O^{2-} interaction (Baniasadi et al., 2014).

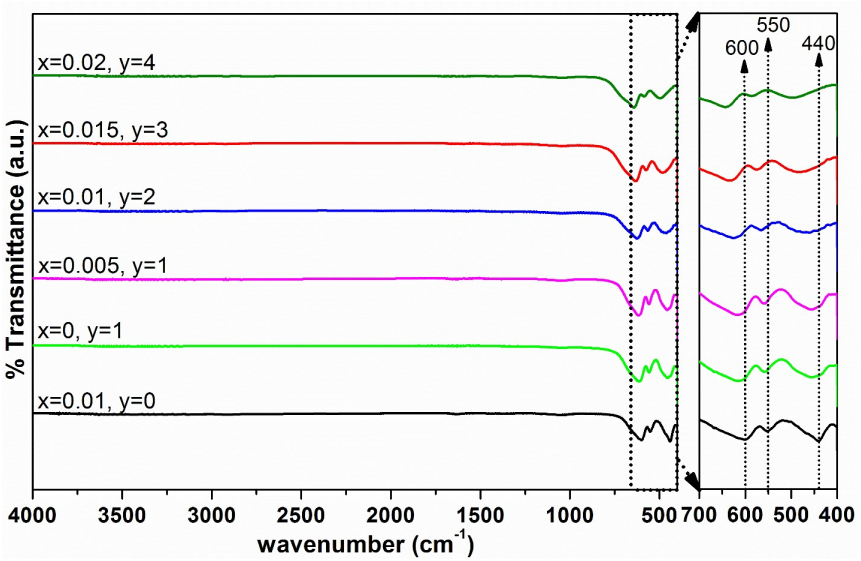

Figure 5.3 *FT-IR spectra of calcined $SrFe_{12-x-y}Ni_xAl_yO_{19}$ ($0.005 \leq x \leq 0.02$; $1 \leq y \leq 4$) hexaferrites.*

Table 5.2 *Characteristic absorption peaks [ν_1, ν_2 (tetrahedral) & ν_3 (octahedral)] and bond length (r) of $SrFe_{12-x-y}Ni_xAl_yO_{19}$ ($0.005 \leq x \leq 0.02$; $1 \leq y \leq 4$) hexaferrites.*

Composition	ν_1 (cm^{-1})	r_1 (Å)	ν_2 (cm^{-1})	r_2 (Å)	ν_3 (cm^{-1})	r_3 (Å)
x=0.01, y=0	600	4.40	550	4.66	440	5.41
x=0, y=1	615	4.33	558	4.62	455	5.29
x=0.005, y=1	615	4.33	558	4.62	455	5.29
x=0.01, y=2	625	4.28	565	4.58	466	5.21
x=0.015, y=3	632	4.25	574	4.53	481	5.10
x=0.02, y=4	642	4.21	585	4.48	496	5.00

All obtained bands (as given in Table 5.2) are in the acceptable range for SrM structure and confirm the satisfactory substitution of Al & Ni ions. In FT-IR spectra, a reverse relationship exists between the wavenumber and atomic weight of the molecule. Replacement of Fe ion (= 55.85 g/mol) by Al ion (= 26.98 g/mol) and Ni ion (= 58.69 g/mol) results in the shifting of characteristic vibration frequencies towards the higher wavenumber according to Hooke's law. This shifting validates the successful substitution of Al & Ni ions in strontium hexaferrite structure.

5.2.3 Densification and Microstructural Properties

The density of all the compositions is estimated by Archimedes' methodology and listed in Table 5.3, along with the porosity. It is observed that the increased substitutional amounts of Ni^{2+} ions are improving the material density. Ni ions possess a significant diffusion coefficient in ferrites which may cause the mass transfer of Ni along the grain boundary and throughout the bulk (Kresse et al., 2013). It might increase the density of the material, which is a factor that favors the M_s enhancement by increasing the magnetic dipoles per unit volume. Furthermore, EDS measurement confirms the presence of Sr, Fe, Ni, Al, and O elements respective to the composition, and their atomic weight percentages are listed in Table 5.3.

Table 5.3 *Atomic weight %, average grain size (G_{avg}), bulk density (BD), and porosity (P) of $SrFe_{12-x-y}Ni_xAl_yO_{19}$ ($0.005 \leq x \leq 0.02$; $1 \leq y \leq 4$) hexaferrites.*

Composition	Atomic weight %					G_{avg}	*BD*	Porosity
	Sr	Fe	Ni	Al	O	(µm)	(g/cm^3)	(%)
x=0.01, y=0	8.10	62.84	0.051	-	29.01	0.47	4.312	15.62
x=0, y=1	8.37	59.18	-	2.54	29.91	0.38	4.270	15.45
x=0.005, y=1	8.34	59.13	0.027	2.53	29.97	0.41	4.285	14.64
x=0.01, y=2	8.63	55.21	0.056	5.29	30.81	0.29	4.304	13.40
x=0.015, y=3	8.89	51.09	0.088	8.18	31.75	0.16	4.356	10.74
x=0.02, y=4	9.17	46.87	0.122	11.31	32.53	0.11	4.371	8.56

Fig. 5.4 shows SEM micrograph of $SrFe_{12-x-y}Ni_xAl_yO_{19}$ ($0.005 \leq x \leq 0.02$; $1 \leq y \leq 4$) hexaferrites. These micrographs confirm the formation of hexagonal platelet-like morphology in all samples. The average grain size is found to reduce with the increasing content of Al^{3+} ions and is shown in Table 5.3. Al ion decreases the mass transportation within the neighboring constituent part during crystal growth. Incorporation of Al^{3+} ion

causes grain size retardation and subsequently increases grain boundaries that are liable for impeding the grain growth in Al-contained samples (Torkian et al., 2016).

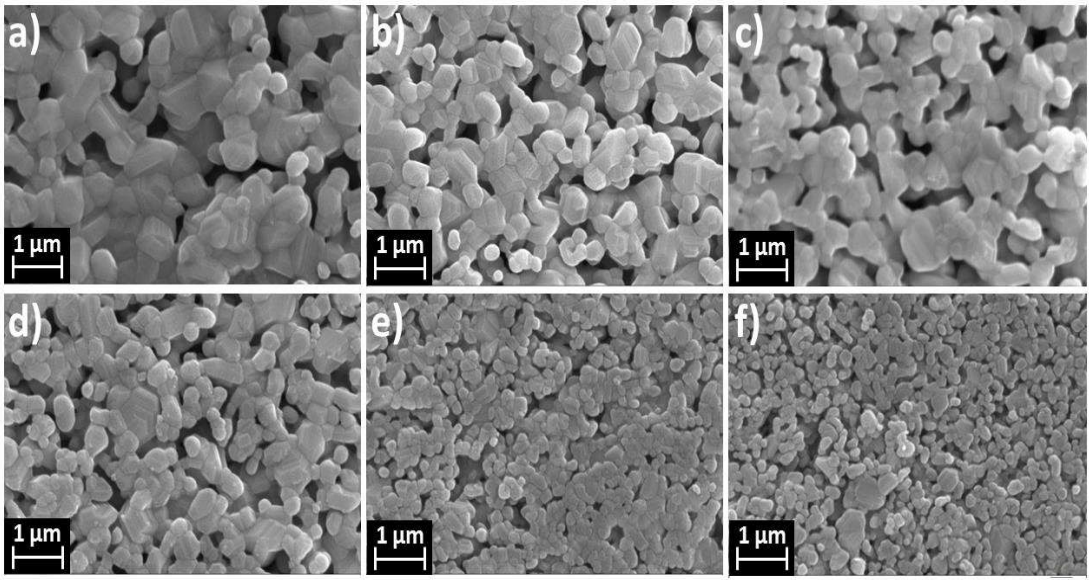

Figure 5.4 *SEM micrographs of a) $SrFe_{11.99}Ni_{0.01}O_{19}$, b) $SrFe_{11}AlO_{19}$, c) $SrFe_{10.995}Ni_{0.005}AlO_{19}$, d) $SrFe_{9.99}Ni_{0.01}Al_2O_{19}$, e) $SrFe_{8.985}Ni_{0.015}Al_3O_{19}$, and f) $SrFe_{7.98}Ni_{0.02}Al_4O_{19}$ hexaferrites.*

Certain amounts of nanoparticles are diffused together, which is resulted from the Fe-Ni diffusion that promotes the self-assembly process of Fe-Ni particle growth (Meng et al., 2020). Fe-Ni ions diffuse together from bulk to the surface under the driving force of segregation energy which is lower on the surface than in bulk. Due to Gibbs free energy, these ions are further reduced, nucleate, and grow into sizes where the size is dependent on the heat treatment time (Meng et al., 2020). The shape anisotropy highly affects the coercivity of a material, which can be visualized in Fig. 1.2. The H_c of nanoscale ferromagnetic particles can be two orders of magnitude larger than that of the bulk material by nano-structuring optimization (Mohapatra & Liu, 2018). The H_c value possibly will decrease for larger grains due to subdivision of grain into domains as well as for smaller grains due to randomizing effects of thermal energy. This way, grain plays a vital role in optimizing the magnetism of nanomaterials.

5.2.4 Magnetic Properties

Fig. 5.5 shows magnetic hysteresis loops of $SrFe_{12-x-y}Ni_xAl_yO_{19}$ ($0.005 \leq x \leq 0.02$; $1 \leq y \leq 4$) hexaferrites at 300 K, and different magnetic parameters are listed in Table 5.4.

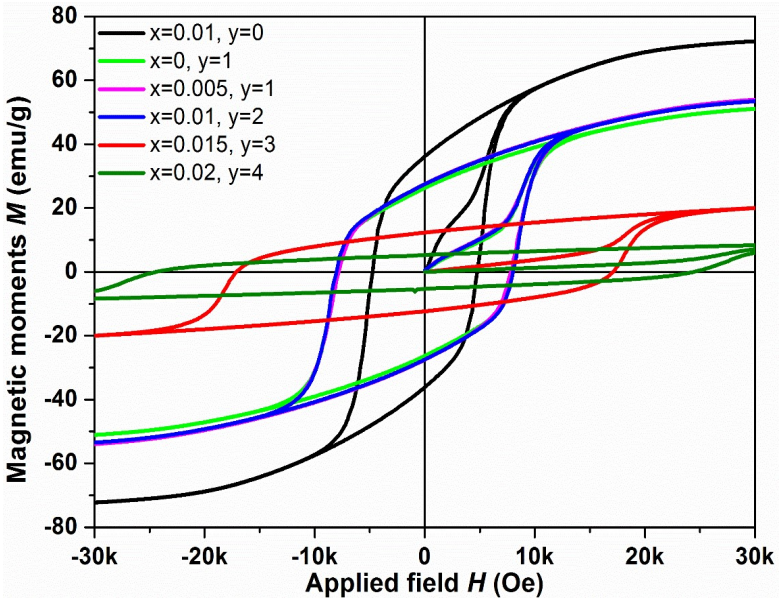

Figure 5.5 *M-H hysteresis curve of $SrFe_{12-x-y}Ni_xAl_yO_{19}$ ($0.005 \leq x \leq 0.02$; $1 \leq y \leq 4$) hexaferrites.*

Table 5.4 *Saturation magnetization (M_s), remanent magnetization (M_r), squareness ratio (M_r/M_s), coercivity (H_c), magnetocrystalline anisotropy field (H_a), and effective magnetic anisotropy (K_{eff}) of $SrFe_{12-x-y}Ni_xAl_yO_{19}$ ($0.005 \leq x \leq 0.02$; $1 \leq y \leq 4$) hexaferrites at 300 K.*

Composition	M_s (emu/g)	M_r (emu/g)	$\frac{M_r}{M_s}$	μ_B	H_c (kOe)	H_a (kOe)	K_{eff} (10^5 erg/g)
$SrFe_{11.99}Ni_{0.01}O_{19}$	72.4	36.16	0.50	13.75	4.76	20.27	7.33
$SrFe_{11}AlO_{19}$	51.1	26.31	0.51	9.45	7.94	21.70	5.54
$SrFe_{10.995}Ni_{0.005}AlO_{19}$	53.9	27.52	0.51	9.97	7.82	21.67	5.84
$SrFe_{9.99}Ni_{0.01}Al_2O_{19}$	53.5	27.46	0.51	9.62	8.01	21.74	5.82
$SrFe_{8.985}Ni_{0.015}Al_3O_{19}$	20.1	12.34	0.61	3.51	17.12	25.39	2.55
$SrFe_{7.98}Ni_{0.02}Al_4O_{19}$	9.9	5.3	0.54	1.68	24.44	34.18	1.69

Saturation magnetization (M_s) values are observed in the range of 9.9-72.4 emu/g. The magnetic moment in SrM is due to the distribution of Fe ions at octahedral [*2a* (↑), *12k*

(↑), *4f₂* (↓)], tetrahedral [*4f₁* (↓)], and trigonal bipyramidal [*2b* (↑)] lattice sites. The minute content of Ni ion in comparison to Al ion shows a decent effect in M_s improvement. Ni^{2+} ($2\mu_B$) ion content is kept very small (up to 0.02) to ensure the *4f₂* lattice site occupancy so that the net magnetization increase in up-spin direction (Mousavi Ghahfarokhi et al., 2015) and results in M_s enhancement. Also, higher Ni ion content is avoided because it can alter the easy magnetization axis and reduce H_c, which is not desirable. Diamagnetic Al^{3+} ion ($0\mu_B$) preferentially replaced paramagnetic Fe^{3+} ion ($5\mu_B$) from *12k* and *2a* lattice sites which reduces the uncompensated upward spins, causing the reduction in M_s value (Wang et al., 2017). The Bohr magnetron number (μ_B) is decreasing with the Al ion content, and the decrease in M_s closely agrees with this varying trend. Al ions in SrM also leads to a non-collinear spin arrangement by reduction in superexchange interaction between $Fe^{3+}_{tetrahedral} - O^{2-} - Fe^{3+}_{octahedral}$. The non-collinear spin coupling with the c-axis aligned core spin can further result in M_s decline (Luo et al., 2012). Fe ions on the *12k* & *2a* lattice site feebly contribute to the magnetocrystalline anisotropy. Hence assimilation of Al ion on *12k* and *2a* sites decreases magnetic anisotropy slightly however reduces M_s significantly, leading to the potential increase in H_c (Sleptsova et al., 2021).

All samples exhibit hard magnetic characteristics as the H_c values are in the range of 4.76-24.44 kOe. H_c is in an increasing pattern with the substitutional content of Al ion. The result is consistent with the SEM analysis, as high H_c is anticipated for smaller grains. The reverse magnetic field for demagnetizing the nanoparticles can be explained by domain rotation, where smaller grains have lesser domain wall movement and hence higher H_c value (Thakur et al., 2013a). Substitution of four Al ions is reported as the legendary way to increase the H_c of the SrM materials by many researchers, such as H_c = 21.3 kOe, M_s = 12.7 emu/g for $Sr_{2/3}Ca_{1/3}Fe_8Al_4O_{19}$ by (Trusov et al., 2018); H_c = 18.1 kOe, M_s = 9 emu/g for $SrFe_8Al_4O_{19}$ by (Luo et al., 2012); H_c = 17.57 kOe, M_s ~ 8 emu/g for $SrFe_8Al_4O_{19}$ by

(Wang et al., 2012). To our knowledge, the highest ever H_c value of 24.44 kOe (M_s = 9.9 emu/g) in SrM-based (rare-earth free) magnet is achieved for the $SrFe_{7.98}Ni_{0.02}Al_4O_{19}$ sample in the present work. This H_c value is even larger than the most famous $Nd_2Fe_{17}B$ (15.07 kOe) permanent magnet. These increments can be justified with the Stoner-Wohlfarth model of magnetization. Magnetocrystalline anisotropy field (H_a) is the physical origin of H_c, which sets the upper limit of H_c that can be realized in a material (Mohapatra & Liu, 2018). However, the observed H_c would always be less than the H_a due to the complex magnetization reversal process. The varying trend of H_c has followed the proportional variation to H_a. Based on the Stoner-Wohlfarth (S-W) theory, the value of magnetocrystalline anisotropy field (H_a) and effective magnetocrystalline anisotropy (K_{eff}) are calculated by Eq. (2.14) [$K_{eff} = M_s\sqrt{(15\gamma/4)} = M_sH_a/2$] (Almessiere et al., 2019) and given in Table 5.4. The value of γ is obtained through the slope of S-W fitting of M vs. $1/H^2$ plot as shown in Fig. 5.6.

The area under the hysteresis loop signifies the total energy absorbed by the material during each cycle. The hysteresis loop shape suggests the magnetic domain behavior and is characterized by the squareness ratio. The square-like shape specifies a high degree of magnetic symmetry in the structure, i.e., it has as many directions as possible toward the easy magnetization axis. A higher degree of squareness ratio is desirable for permanent magnet applications. The squareness ratio (M_r/M_s) is found to be $\geq$ 0.5 for all the compositions that confirm the single-magnetic domain formation in the samples. The formation of a single-domain obstructs the domain-wall motion and demagnetization process by coherent spin rotation and hence leads to the H_c improvement (Torkian et al., 2016; Trusov et al., 2018). In a ferromagnetic material, maximum H_c can be managed by refining the particle size to a single-domain region. Magnetization reversal by coherent rotation of magnetic vector against the magnetocrystalline anisotropy from one easy axis

to another results in maximum H_c in single-domain particles. The Stoner-Wohlfarth model specifies that if the magnetization reversal process occurs in the particle by coherent reverse mode, the remanent magnetization (M_r) value will be half of the M_s. A large value of M_r can be attained by easy axis alignment, and increasing magnetic intergranular interaction. The M_r values of compositions are observed between 5.3-36.16 emu/g, which is higher than half of the M_s value. High M_r and high H_c are the fundamental parameters for the large energy density in a permanent magnet, which is desirable for efficient PM applications.

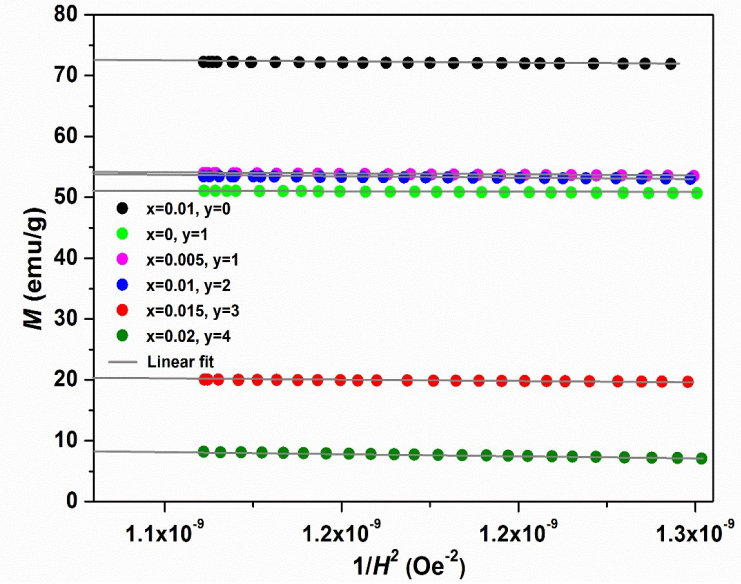

Figure 5.6.*M vs $1/H^2$ plot with linear fit for $SrFe_{12-x-y}Ni_xAl_yO_{19}$ ($0.005 \leq x \leq 0.02$; $1 \leq y \leq 4$) hexaferrites.*

5.2.5 Dielectric Properties

Dielectric characteristic plays a vital role in advanced applications. Frequency-dependent characteristics of dielectric constant (ε) are recorded at room temperature for $SrFe_{12-x-y}Ni_xAl_yO_{19}$ ($0.005 \leq x \leq 0.02$; $1 \leq y \leq 4$) and shown in Fig. 5.7. The values of dielectric parameters (ε, $tan\delta$) at 1 MHz frequency are listed in Table 5.5.

The intrinsic dielectric response of strontium hexaferrite (ferromagnetic material, space group $P6_3/mmc$) is related to crystal structure consisting of two electric dipoles

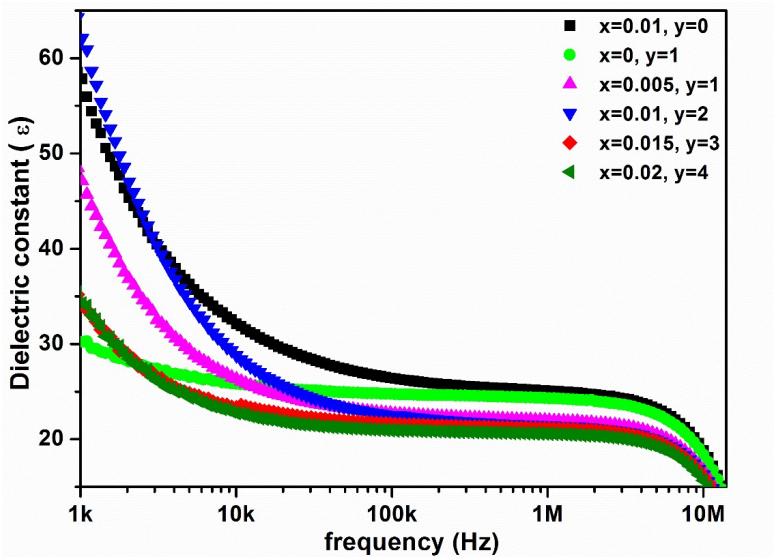

Figure 5.7 *Dielectric constant (ε) of $SrFe_{12-x-y}Ni_xAl_yO_{19}$ ($0.005 \leq x \leq 0.02$; $1 \leq y \leq 4$) hexaferrites with respect to frequency at room-temperature.*

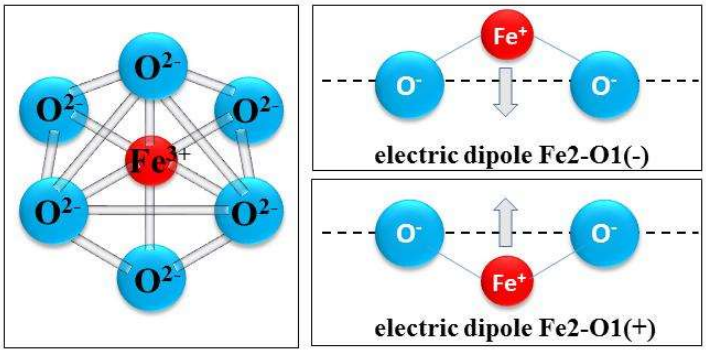

Figure 5.8 *Schematic of polarization occurrence due to distorted oxygen octahedron.*

Table 5.5 *Room-temperature value of dielectric constant (ε), tangent loss (tanδ), resistivity (ρ), and conductivity (σ) of $SrFe_{12-x-y}Ni_xAl_yO_{19}$ ($0.005 \leq x \leq 0.02$; $1 \leq y \leq 4$) hexaferrites at 1MHz frequency.*

Composition	ε	$tan\delta$	ρ (10^6 Ω-cm)	σ (10^{-7} S-cm^{-1})
x=0.01, y=0	25.09	0.0244	2.86	3.50
x=0, y=1	24.32	0.0111	6.50	1.54
x=0.005, y=1	21.97	0.0161	4.96	2.02
x=0.01, y=2	21.43	0.0097	8.46	1.18
x=0.015, y=3	21.12	0.0092	9.01	1.11
x=0.02, y=4	20.57	0.0048	17.56	0.57

switchable along the *c*-axis in a unit cell; a schematic representation of dipoles is shown in Fig. 5.8. The shift of ferric ion Fe2 (towards O1) below the mirror plane m is equivalent to electric dipole Fe2-O1(-) oriented in an antiparallel direction to the *c*-axis. In contrast, the mirror-plane displacement of Fe2 (towards O1) above the mirror plane m is equivalent to electric dipole Fe2-O1(+) oriented in a parallel direction to the *c*-axis (Hilczer & Pasińska, 2022). The extrinsic dielectric response depends on the microstructure of grain and heterogeneous ceramic structure. The effect of heterogeneous ceramic structure can be explained by Maxwell-Wagner and Koop model. According to these models, the structure of hexaferrite materials consists of two layers, highly conducting grains and poorly conducting grain boundaries. Space charge gets accumulated at grain boundaries under an externally applied electric field, and transfer of electrons occurs in the external electric field direction resulting in dielectric polarization.

All compositions represent the typical dielectric characteristic of ferrites, i.e., acute decrease in dielectric parameters with increasing frequency of applied electric field (Mousavi Ghahfarokhi et al., 2015). Dielectric dispersion results from electronic, ionic, dipolar, and interfacial polarization, in which the latter two are significant at low frequencies. The ε value is high at low frequencies due to the accumulation of space charge polarization at highly resistive grain boundaries. Space charge carriers need a finite time to reorganize their axes parallel to the ac electric field. Hence, the transfer of electrons between Fe ions cannot follow the ac field with the increasing frequency of externally applied electric field, resulting in a decrease of dielectric constant at higher frequencies. At high frequencies, ε originates from conducting grain layer and results in a low dielectric constant. With the increasing content of Ni-Al ions, both dielectric constant and tangent loss is observed in decreasing pattern. The decrease is due to the substitutional preference of Al^{3+} (*12k*, *2a*) and Ni^{2+} ($4f_2$) ions at the octahedral lattice site (Mousavi Ghahfarokhi et

al., 2015; Wang et al., 2017). Predominantly, octahedral lattice sites contribute to the conduction mechanism in hexaferrite due to the hopping of electrons at this site (Ashiq et al., 2011) because the probability of electron hopping between octahedral-octahedral sites is higher than the octahedral-tetrahedral and tetrahedral-tetrahedral sites. Substitution of Ni-Al ions decreases the Fe ions and the hopping of electrons at octahedral sites, resulting in the declining value of dielectric parameters with Ni-Al cation content. The processing methods, chemical stoichiometry, heat treatments, grain sizes, and charge carriers strongly affect the dielectric properties of materials. The ε of a material is inversely proportional to the square root of the resistance caused by grains and grain boundaries (Thakur et al., 2013b). The smaller grains and, therefore larger grain boundaries with the increasing content of Ni-Al ions are also a reason for the variation of ε as observed in the compositions, which is consistent with the microstructural results.

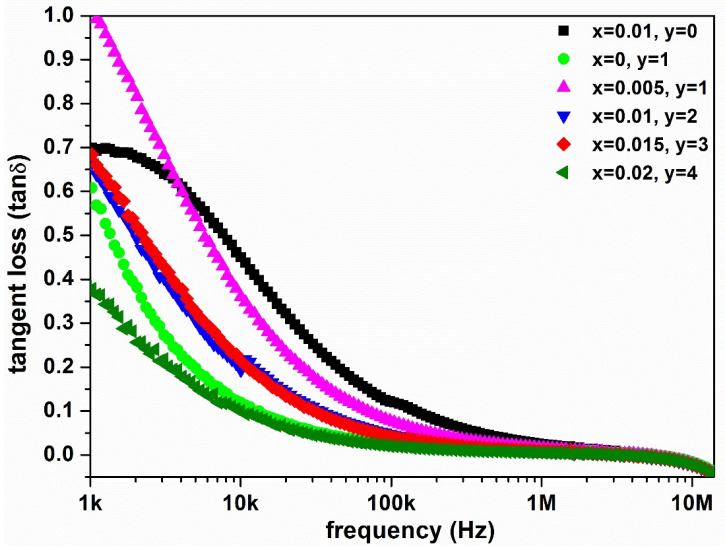

Figure 5.9 *Dielectric loss (tanδ) of $SrFe_{12-x-y}Ni_xAl_yO_{19}$ ($0.005 \leq x \leq 0.02$; $1 \leq y \leq 4$) hexaferrites with respect to frequency at room-temperature.*

In a dielectric material, losses arise because of the work-done required to overcome the frictional damping force encountered by dipole rotation (Ashiq et al., 2009). Dielectric tangent loss (*tanδ*) is recorded at room temperature for $SrFe_{12-x-y}Ni_xAl_yO_{19}$ ($0.005 \leq x \leq$

0.02; $1 \leq y \leq 4$) and shown in Fig 5.9. It signifies the energy dissipation in the material and shows a declining behavior with increasing frequency. Due to highly resistive grain boundaries, more energy is required for electron exchange between Fe ions at low frequencies. It causes high energy loss, and as a result, a high value of tanδ at low frequencies is obtained. In a high-frequency region, highly conducting grains become dominant, which reduces the energy requirement of electron transfer among Fe ions and hence low energy loss, resulting in a low $tan\delta$ value.

5.2.6 Electrical Properties

The electrical properties in ferrites are caused by electron hopping between ions of the same element present in more than one different oxidation state. The room-temperature variation of resistivity (ρ) with the frequency is shown in Fig. 5.10. The resistivity characteristic is observed in decreasing mode with the increasing frequency because electrons gain the threshold hopping energy at higher frequencies that increase the conduction mechanism in the material (Ahmad et al., 2016). The resistivity and ac conductivity at 1 MHz frequency is tabulated in Table 5.5. The ac conductivity (σ) behavior is studied to correlate the conduction-mechanism and dielectric-relaxation phenomenon. Electron transfer, polarization, valence variation, oxygen vacancy, and grain defects affect the conduction mechanism in ferrites (Auwal et al., 2016). In Fig. 5.10, ρ is decreasing with the increasing frequency, and correspondingly conductivity is expected to increase due to the reciprocal relationship ($\sigma = 1/\rho$). Grain boundaries are the energy mismatch regions between two adjacent grains that are resistive in nature and act as a barrier to electron movement. Smaller grains increase the grain boundaries, which reduces the conduction mechanism. Due to the increasing substitutional amount of Ni-Al ion, the smaller grain and hence larger grain boundaries of samples cause the high value of resistivity and correspondingly low conductivity as observed in the samples.

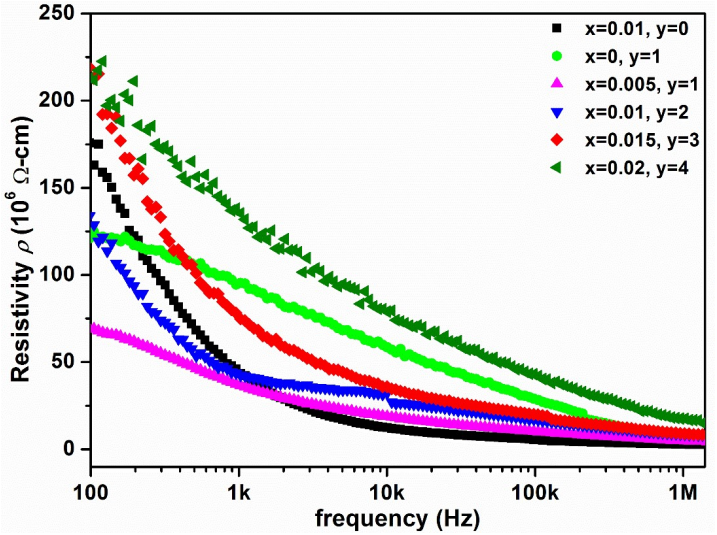

Figure 5.10 *Frequency-dependent resistivity variation in $SrFe_{12-x-y}Ni_xAl_yO_{19}$ ($0.005 \leq x \leq 0.02$; $1 \leq y \leq 4$) hexaferrites.*

5.3 Conclusions

The composition of $SrFe_{12-x-y}Ni_xAl_yO_{19}$ ($0.005 \leq x \leq 0.02$; $1 \leq y \leq 4$) is successfully synthesized by the sol-gel auto-combustion process. The structural, magnetic, and dielectric properties are carried out to explore the application scope of these modified SrM-based magnets. It is found that the substitution of Ni-Al ions can improve the hard magnetism of strontium hexaferrite magnets. Substitution of Ni^{2+} ion is observed to increase the M_s value of the composition without adversely affecting the H_c property. Substitution of Al^{3+} ion is found liable for smaller grain sizes and higher H_c in the samples. In the $SrFe_{8.985}Ni_{0.015}Al_3O_{19}$ composition, a H_c value of 17.12 kOe is obtained with 20.1 emu/g of M_s value, which is anticipated to be suitable for different PM applications. This magnet can be proposed to reduce the dependency on rare-earth-contained permanent magnets, especially for motor applications (~45% application share of PM). In this series, the highest ever H_c value of 24.44 kOe in SrM-based (rare-earth free) magnet is attained for the $SrFe_{7.98}Ni_{0.02}Al_4O_{19}$ composition with M_s of 9.9 emu/g. In addition to such magnetic properties, these magnets also offer high resistivity, negligible eddy current loss, high

oxidation and corrosion resistance, which is practically desirable for efficient PM applications. Further improvisation in these magnets can be a revolutionary breakthrough in the magnet industry which is passionately searching for a rare-earth free strong permanent magnet comparable to the property of the NdFeB magnet.